

REPORT DOCUMENTATION PAGE

Form Approved
OMB No. 0704-0188

Public reporting burden for this collection of information is estimated to average 1 hour per response, including the time for reviewing instructions, searching existing data sources, gathering and maintaining the data needed, and completing and reviewing this collection of information. Send comments regarding this burden estimate or any other aspect of this collection of information, including suggestions for reducing this burden to Department of Defense, Washington Headquarters Services, Directorate for Information Operations and Reports (0704-0188), 1215 Jefferson Davis Highway, Suite 1204, Arlington, VA 22202-4302. Respondents should be aware that notwithstanding any other provision of law, no person shall be subject to any penalty for failing to comply with a collection of information if it does not display a currently valid OMB control number. **PLEASE DO NOT RETURN YOUR FORM TO THE ABOVE ADDRESS.**

1. REPORT DATE (DD-MM-YYYY) 30-Sep-2008		2. REPORT TYPE REPRINT		3. DATES COVERED (From - To)	
4. TITLE AND SUBTITLE REFINED LOCAL AND REGIONAL SEISMIC VELOCITY AND ATTENUATION MODELS FROM FINITE-FREQUENCY WAVEFORMS				5a. CONTRACT NUMBER FA8718-06-C-0014	
				5b. GRANT NUMBER	
				5c. PROGRAM ELEMENT NUMBER 62601F	
6. AUTHOR(S) Wei Zhang ¹ , Yang Shen ² , Li Zhao ³ , and Xiaoping Yang ¹				5d. PROJECT NUMBER 1010	
				5e. TASK NUMBER SM	
				5f. WORK UNIT NUMBER A1	
7. PERFORMING ORGANIZATION NAME(S) AND ADDRESS(ES) Science Applications International Corporation 10260 Campus Point Drive San Diego, CA 92121-1152				8. PERFORMING ORGANIZATION REPORT NUMBER	
9. SPONSORING / MONITORING AGENCY NAME(S) AND ADDRESS(ES) Air Force Research Laboratory 29 Randolph Road Hanscom AFB, MA 01731-3010				10. SPONSOR/MONITOR'S ACRONYM(S) AFRL/RVBYE	
				11. SPONSOR/MONITOR'S REPORT NUMBER(S) AFRL-RV-HA-TR-2008-1087	
12. DISTRIBUTION / AVAILABILITY STATEMENT Approved for Public Release; Distribution Unlimited. Science Applications International Corporation ¹ , University of Rhode Island ² , and Institute of Earth Sciences, Academia Sinica, Taiwan ³					
13. SUPPLEMENTARY NOTES Reprinted from: Proceedings of the 30 th Monitoring Research Review – Ground-Based Nuclear Explosion Monitoring Technologies, 23 – 25 September 2008, Portsmouth, VA, Volume I pp 316 - 325.					
14. ABSTRACT In seismic tomography, the reference or starting models are commonly one-dimensional (1D) and the structural sensitivity kernels of seismic data are calculated without considering the finiteness of seismic waves in both time and frequency domains. These simplifications result in a theoretical limit, in addition to that from the data coverage, on the structural resolution in tomography inversions. In small-scale (such as the crustal) structural imaging, however, a higher resolution is desired, and the 1D reference model is no longer adequate; therefore, accurate modeling of wave propagation in three-dimensional (3D) reference models is necessary. To address this problem, elaborate numerical methods, such as the finite-difference and spectral-element methods, have been adopted to calculate the full-wave, finite-frequency, banana-doughnut, structural sensitivity kernels of seismic data. The objective of this work is to develop refined local and regional velocity and attenuation models for selected areas of interest (AOIs) in Eurasia. We have carried out systematic tests to validate the finite-frequency sensitivity kernels computed by a staggered-grid, finite-difference method. These tests result in corrections in the calculation of the structural sensitivity kernels as well as an important finding that anomalies in S-wave speed have a significant contribution to P-wave traveltime perturbations (Zhang and Shen, 2008). Thus, current seismic tomography practices, in which P-wave traveltimes are assumed to be unrelated to S-wave velocity anomalies, may lead to systematic biases in inversion results. Furthermore, the different components of the same arrival at the same receiver have different traveltime and amplitude sensitivities to variations in the velocity structure (Shen et al., 2008). We have applied our finite-difference-based full-wave, finite-frequency approach to obtain a refined structural model in Eastern Turkey. We continue the application of our finite-frequency approach in the refinement of the seismic velocity and attenuation models and focus on the Iran region. Our previous full-wave approach has been based on the finite-difference algorithm in a Cartesian coordinate system. However, the Iran region under current study is relatively large so that the Earth's curvature effect on wave propagation cannot be ignored. Thus, we developed an alternative finite-difference algorithm that solves the seismic-wave equation in the polar-spherical coordinate system on a non-staggered and non-uniform grid. We have also validated this algorithm by comparing its synthetic seismograms with those calculated by normal-mode summation. Our tomography study covers the region 39°E-66°E and 22°N-44°N, with a depth range of 0–700 km. Waveform records from regional events and stations were collected. For initial tomographic iterations, we selected 31 larger earthquakes at 16 stations belonging to the Iran National Seismic Network. Their source mechanisms are available from the Harvard CMT solutions, though we use the revised locations determined by Engdahl and Bergman (personal communication). We used the regional a priori 3D geophysical model of Pasyanos et al. (2004) as our starting model and applied the spherical finite-difference algorithm to compute the synthetic seismograms. Frequency-dependent anomalies in phase and amplitude are measured by the cross-correlation between synthetic and recorded seismograms. Full-wave, finite-frequency structural sensitivity kernels of these measurements are calculated by the spherical finite-difference scheme. The final 3D structural model for the Iran region will be obtained through a non-linear iterative process in which the inversion results from each iteration will serve as the reference model for the next iteration.					
15. SUBJECT TERMS Seismic characterization, Seismic propagation					
16. SECURITY CLASSIFICATION OF:			17. LIMITATION OF ABSTRACT SAR	18. NUMBER OF PAGES 10	19a. NAME OF RESPONSIBLE PERSON Robert J. Raistrick
a. REPORT UNCLAS	b. ABSTRACT UNCLAS	c. THIS PAGE UNCLAS			19b. TELEPHONE NUMBER (include area code) 781-377-3726

REFINED LOCAL AND REGIONAL SEISMIC VELOCITY AND ATTENUATION MODELS FROM
FINITE-FREQUENCY WAVEFORMS

Wei Zhang², Yang Shen², Li Zhao³, and Xiaoping Yang¹

Science Applications International Corporation¹, University of Rhode Island²,
and Institute of Earth Sciences, Academia Sinica, Taiwan³

Sponsored by Air Force Research Laboratory

Contract No. FA8718-06-C-0014

Proposal No. BAA06-60

ABSTRACT

In seismic tomography, the reference or starting models are commonly one-dimensional (1D) and the structural sensitivity kernels of seismic data are calculated without considering the finiteness of seismic waves in both time and frequency domains. These simplifications result in a theoretical limit, in addition to that from the data coverage, on the structural resolution in tomography inversions. In small-scale (such as the crustal) structural imaging, however, a higher resolution is desired, and the 1D reference model is no longer adequate; therefore, accurate modeling of wave propagation in three-dimensional (3D) reference models is necessary. To address this problem, elaborate numerical methods, such as the finite-difference and spectral-element methods, have been adopted to calculate the full-wave, finite-frequency, banana-doughnut, structural sensitivity kernels of seismic data.

The objective of this work is to develop refined local and regional velocity and attenuation models for selected areas of interest (AOIs) in Eurasia. We have carried out systematic tests to validate the finite-frequency sensitivity kernels computed by a staggered-grid, finite-difference method. These tests result in corrections in the calculation of the structural sensitivity kernels as well as an important finding that anomalies in S-wave speed have a significant contribution to P-wave traveltimes perturbations (Zhang and Shen, 2008). Thus, current seismic tomography practices, in which P-wave traveltimes are assumed to be unrelated to S-wave velocity anomalies, may lead to systematic biases in inversion results. Furthermore, the different components of the same arrival at the same receiver have different traveltimes and amplitude sensitivities to variations in the velocity structure (Shen et al., 2008). We have applied our finite-difference-based full-wave, finite-frequency approach to obtain a refined structural model in Eastern Turkey.

We continue the application of our finite-frequency approach in the refinement of the seismic velocity and attenuation models and focus on the Iran region. Our previous full-wave approach has been based on the finite-difference algorithm in a Cartesian coordinate system. However, the Iran region under current study is relatively large so that the Earth's curvature effect on wave propagation cannot be ignored. Thus, we developed an alternative finite-difference algorithm that solves the seismic-wave equation in the polar-spherical coordinate system on a non-staggered and non-uniform grid. We have also validated this algorithm by comparing its synthetic seismograms with those calculated by normal-mode summation. Our tomography study covers the region 39°E-66°E and 22°N-44°N, with a depth range of 0-700 km. Waveform records from regional events and stations were collected. For initial tomographic iterations, we selected 31 larger earthquakes at 16 stations belonging to the Iran National Seismic Network. Their source mechanisms are available from the Harvard CMT solutions, though we use the revised locations determined by Engdahl and Bergman (personal communication). We used the regional a priori 3D geophysical model of Pasyanos et al. (2004) as our starting model and applied the spherical finite-difference algorithm to compute the synthetic seismograms. Frequency-dependent anomalies in phase and amplitude are measured by the cross-correlation between synthetic and recorded seismograms. Full-wave, finite-frequency structural sensitivity kernels of these measurements are calculated by the spherical finite-difference scheme. The final 3D structural model for the Iran region will be obtained through a non-linear iterative process in which the inversion results from each iteration will serve as the reference model for the next iteration.

20081014130

OBJECTIVES

In this work we obtain Finite-Frequency Seismic Tomography (FFST) velocity models for Eurasia and use them as 3D reference models to refine crustal and shallow upper mantle velocity and attenuation models for focused AOIs by applying the fully 3D tomography approach.

RESEARCH ACCOMPLISHED

Development of Non-Staggered, Non-Uniform Grid Finite-Difference Algorithm in Spherical Geometry

In our research accomplished in the previous year, we focused on the 3D crustal structure in eastern Turkey and northern Iran and carried out a finite-frequency tomography inversion based on a 3D reference crustal model based on MENA 1.1 (Walter et al. 2000). We used a fourth-order staggered-grid finite-difference algorithm (Olsen 1994) to compute the synthetic seismograms in the layered crustal model with variable Moho depth. The crustal model has a minimum shear-wave speed of 1.1 km/s. In our finite-difference simulations, we used a uniform grid spacing of 300 m, resulting in reliable waveforms up to a nominal frequency of about 0.5 Hz.

Like most implementations of the finite-difference method, the staggered-grid finite-difference algorithm of Olsen (1994) we used in a previous study has been designed for rectangular geometry in the Cartesian coordinate system where the Earth's sphericity has been ignored. This is acceptable when the modeling area is small so that the paths of regional seismic waves are relatively short. In this year's research, however, we expanded our area of interest to the entire area of Iran and the surrounding region. As a result of the much larger modeling area, the paths of the seismic wave involved are often longer so that the effect of the Earth's curvature on seismic wave propagation needs to be taken into account. A simple approach to account for the Earth's sphericity is to make a so-called Earth-flattening transformation. It has often been applied in asymptotic treatment of wave propagation in the spherical Earth (Chapman and Orcutt 1985). However, the transformation is inexact, and the errors it causes in waveforms have not been quantitatively studied.

Here, we choose to develop an implementation of the finite-difference method in the polar spherical coordinate system so that the propagation of seismic waves in the 3D structure of a spherical Earth can be modeled accurately. We use the geocentric spherical coordinate (GSC) system in which the origin is located at the center of the Earth and the three coordinate variables are co-latitude θ , azimuth φ , and radius r . The conversion between the GSC system and the geocentric Cartesian system is

$$\begin{aligned}\theta &= \arctan\left(\frac{\sqrt{x^2 + y^2}}{z}\right), \\ \varphi &= \arctan(y/x), \\ r &= \sqrt{x^2 + y^2 + z^2}.\end{aligned}\tag{1}$$

The elastic wave equation we solve can be written in the velocity-stress form:

$$\rho \mathbf{v}_{,t} = \nabla \cdot \boldsymbol{\sigma} + \mathbf{f},\tag{2}$$

where the stress-rate tensor can be expressed via the Hooke's law

$$\dot{\boldsymbol{\sigma}} = \mathbf{C} : \left\{ \frac{1}{2} [(\nabla \mathbf{v}) + (\nabla \mathbf{v})^T] \right\}.\tag{3}$$

In the GSC system, these equations can be explicitly written as

$$\begin{aligned}\rho v_{\theta,t} &= \frac{1}{r} \sigma_{\theta\theta,\theta} + \frac{1}{r \sin \theta} \sigma_{\theta\varphi,\varphi} + \sigma_{\theta r,r} + \frac{1}{r} (3\sigma_{\theta r} + \sigma_{\theta\theta} \cot \theta - \sigma_{\varphi\varphi} \cot \theta), \\ \rho v_{\varphi,t} &= \frac{1}{r} \sigma_{\theta\varphi,\theta} + \frac{1}{r \sin \theta} \sigma_{\varphi\varphi,\varphi} + \sigma_{\varphi r,r} + \frac{1}{r} (2\sigma_{\theta\varphi} \cot \theta - 3\sigma_{\varphi r} \cot \theta), \\ \rho v_{r,t} &= \frac{1}{r} \sigma_{\theta r,\theta} + \frac{1}{r \sin \theta} \sigma_{\varphi r,\varphi} + \sigma_{rr,r} + \frac{1}{r} (2\sigma_{rr} - \sigma_{\theta\theta} - \sigma_{\varphi\varphi} + \sigma_{\theta r} \cot \theta),\end{aligned}\tag{4}$$

$$\begin{aligned}
 \dot{\sigma}_{\theta\theta} &= \frac{\lambda}{r}(v_{\theta} \cot \theta + \frac{1}{\sin \theta} v_{\varphi, \varphi} + v_r) + \frac{\lambda + 2\mu}{r}(v_{\theta, \theta} + v_r) + \lambda v_{r, r}, \\
 \dot{\sigma}_{\varphi\varphi} &= \frac{\lambda + 2\mu}{r}(v_{\theta} \cot \theta + \frac{1}{\sin \theta} v_{\varphi, \varphi} + v_r) + \frac{\lambda}{r}(v_{\theta, \theta} + v_r) + \lambda v_{r, r}, \\
 \dot{\sigma}_{rr} &= \frac{\lambda}{r}(v_{\theta} \cot \theta + \frac{1}{\sin \theta} v_{\varphi, \varphi} + v_r) + \frac{\lambda}{r}(v_{\theta, \theta} + v_r) + (\lambda + 2\mu)v_{r, r}, \\
 \dot{\sigma}_{\theta\varphi} &= \frac{\mu}{2r}(v_{\varphi, \theta} + \frac{1}{\sin \theta} v_{\theta, \varphi} - v_{\varphi} \cot \theta), \\
 \dot{\sigma}_{\theta r} &= \frac{\mu}{2}(\frac{1}{r} v_{r, \theta} + v_{\theta, r} - \frac{1}{r} v_{\theta}), \\
 \dot{\sigma}_{\varphi r} &= \frac{\mu}{2}(\frac{1}{r \sin \theta} v_{r, \varphi} + v_{\varphi, r} - \frac{1}{r} v_{\varphi}).
 \end{aligned} \tag{5}$$

The free-surface boundary condition can also be expressed in the GSC system as

$$\sigma_{\theta r} = 0, \quad \sigma_{\varphi r} = 0, \quad \sigma_{rr} = 0. \tag{6}$$

One of the drawbacks of many finite-difference implementations in modeling seismic wave propagation is the requirement that the grid size be constant in all three spatial directions and everywhere in the modeling volume. When the seismic wave speed varies over a wide range, the efficiency of the finite-difference scheme is drastically reduced. This happens when the S-wave speed is very low near the surface, such as in a sedimentary basin, where a very small grid size is needed. If a uniform grid is required, then the same small grid size is used in the deeper part of the model where the wave speed is much higher and a small grid size may not be needed. To address this problem in order to increase the efficiency of the finite-difference algorithm, we developed a non-uniform grid approach in which the coordinates (θ, φ, r) of the uniform grid points are transformed to the coordinates of points on a non-uniform grid, denoted by (ξ, η, ζ) , via the relations:

$$\theta = \theta(\xi), \quad \varphi = \varphi(\eta), \quad r = r(\zeta). \tag{7}$$

The derivatives of these transformation relations can be calculated by the same differencing operator D used in the finite-difference algorithm

$$\theta_{, \xi} = D_{\xi} \theta, \quad \varphi_{, \eta} = D_{\eta} \varphi, \quad r_{, \zeta} = D_{\zeta} r. \tag{8}$$

Therefore, the velocity-stress form of the elastic wave equations (4) and (5) become

$$\begin{aligned}
 \rho v_{\theta, t} &= \frac{1}{r} \xi_{, \theta} \sigma_{\theta\theta, \xi} + \frac{1}{r \sin \theta} \eta_{, \varphi} \sigma_{\theta\varphi, \eta} + \zeta_{, r} \sigma_{\theta r, \zeta} + \frac{1}{r} (3\sigma_{\theta r} + \sigma_{\theta\theta} \cot \theta - \sigma_{\varphi\varphi} \cot \theta), \\
 \rho v_{\varphi, t} &= \frac{1}{r} \xi_{, \theta} \sigma_{\theta\varphi, \xi} + \frac{1}{r \sin \theta} \eta_{, \varphi} \sigma_{\varphi\varphi, \eta} + \zeta_{, r} \sigma_{\varphi r, \zeta} + \frac{1}{r} (2\sigma_{\theta\varphi} \cot \theta - 3\sigma_{\varphi r} \cot \theta), \\
 \rho v_{r, t} &= \frac{1}{r} \xi_{, \theta} \sigma_{\theta r, \xi} + \frac{1}{r \sin \theta} \eta_{, \varphi} \sigma_{\varphi r, \eta} + \zeta_{, r} \sigma_{rr, \zeta} + \frac{1}{r} (2\sigma_{rr} - \sigma_{\theta\theta} - \sigma_{\varphi\varphi} + \sigma_{\theta r} \cot \theta),
 \end{aligned} \tag{9}$$

$$\begin{aligned}
 \dot{\sigma}_{\theta\theta} &= \frac{\lambda}{r}(v_{\theta} \cot \theta + \frac{1}{\sin \theta} \eta_{, \varphi} v_{\varphi, \eta} + v_r) + \frac{\lambda + 2\mu}{r}(\xi_{, \theta} v_{\theta, \xi} + v_r) + \lambda \zeta_{, r} v_{r, \zeta}, \\
 \dot{\sigma}_{\varphi\varphi} &= \frac{\lambda + 2\mu}{r}(v_{\theta} \cot \theta + \frac{1}{\sin \theta} \eta_{, \varphi} v_{\varphi, \eta} + v_r) + \frac{\lambda}{r}(\xi_{, \theta} v_{\theta, \xi} + v_r) + \lambda \zeta_{, r} v_{r, \zeta}, \\
 \dot{\sigma}_{rr} &= \frac{\lambda}{r}(v_{\theta} \cot \theta + \frac{1}{\sin \theta} \eta_{, \varphi} v_{\varphi, \eta} + v_r) + \frac{\lambda}{r}(\xi_{, \theta} v_{\theta, \xi} + v_r) + (\lambda + 2\mu)\zeta_{, r} v_{r, \zeta}, \\
 \dot{\sigma}_{\theta\varphi} &= \frac{\mu}{2r}(\xi_{, \theta} v_{\varphi, \xi} + \frac{1}{\sin \theta} \eta_{, \varphi} v_{\theta, \eta} - v_{\varphi} \cot \theta), \\
 \dot{\sigma}_{\theta r} &= \frac{\mu}{2}(\frac{1}{r} \xi_{, \theta} v_{r, \xi} + \zeta_{, r} v_{\theta, \zeta} - \frac{1}{r} v_{\theta}), \\
 \dot{\sigma}_{\varphi r} &= \frac{\mu}{2}(\frac{1}{r \sin \theta} \eta_{, \varphi} v_{r, \eta} + \zeta_{, r} v_{\varphi, \zeta} - \frac{1}{r} v_{\varphi}),
 \end{aligned} \tag{10}$$

with the free-surface boundary conditions for stress and velocity components (from equations 6 and 10):

$$\begin{aligned}
 \zeta_{,r} v_{\theta,\zeta} &= \frac{1}{r} (-\xi_{,\theta} v_{r,\xi} + v_{\theta}), \\
 \zeta_{,r} v_{r,\zeta} &= -\frac{\lambda}{\lambda + 2\mu} \frac{1}{r} (\xi_{,\theta} v_{\theta,\xi} + v_{\theta} \cot \theta + \frac{1}{\sin \theta} \eta_{,\phi} v_{\phi,\eta} + 2v_r), \\
 \zeta_{,r} v_{\phi,\zeta} &= -\frac{1}{r \sin \theta} \eta_{,\phi} v_{r,\eta} + \frac{1}{r} v_{\phi}.
 \end{aligned} \tag{11}$$

We have implemented this spherical, non-uniform grid approach. A number of experiments have been conducted to validate the code by comparing the simulation results with the synthetics calculated by normal-mode summation. Figure 1 shows a few examples of the comparisons of the finite-difference and normal-mode synthetic seismograms. This alternative implementation of the finite-difference method enables us to efficiently and accurately model the propagation of seismic waves in a spherical Earth with 3D variations in seismic wave speeds. As a first application of this finite-difference algorithm, we use it to conduct a full-wave, finite-frequency tomography for the Iran region.

Full-Wave, Finite-frequency Tomography for the Iran Region

Iran is located in a seismically active region with frequent and widely distributed moderate-sized earthquakes (see Figure 2). Yet there has been a paucity of detailed investigation of the seismic structure of the crust and uppermost mantle in this region. Occasional seismic interests in this region included crustal studies using the Pn waves (e.g., Chen et al. 1980; Asudeh 1982; Hearn and Ni 1994; Ritzwoller et al. 2002) and uppermost mantle tomography studies (e.g., Ritzwoller and Levshin 1998; Ritzwoller et al. 1998; Maggi and Priestley 2005). In all the tomography studies, the Iran region is merely a portion of the larger model, and is characterized by a single swath of low-velocity region without internal structure. Therefore, a more focused study using local earthquakes and stations is necessary to obtain a refined 3D structure.

We selected the region between 22°N and 44°N and between 39°E and 66°E for our full-wave, finite-frequency tomography. For the reference or starting model, we chose the regional a priori 3D geophysical model of Pasyanos et al. (2004). This 3D model is constructed by combining the results from a number of published structural studies rather than from tomographic inversions. The resulting model includes density and the velocities and quality factors of P and S waves specified on a 1°x1° horizontal grid and at 24 depths from 0 to 660 km. Figure 3 shows a few map views and profiles of the 3D reference model.

We used the non-staggered grid finite-difference algorithm described in the previous section to compute the synthetic seismograms as well as the Fréchet kernels for tomography inversions. We stripped the water from the reference model by uniformly extending the structure right beneath the water up to the surface and imposed a minimum shear-wave speed of 1.2 km/s. Since most of the event-station paths are off the water/sediment covered areas (Figure 3), this approximation reduces computation with a minimum loss of accuracy in synthetic waveforms. A more refined grid can be applied to sediment-covered areas in following iterations of solution. In our finite-difference simulations, we used a time step of 0.12 s, a horizontal grid spacing of 0.02°, and a vertically variable grid spacing of 1–7.5 km, as shown in Figure 4, resulting in reliable surface waveforms up to a nominal period of about 15 s for event-station paths through the water/sediment covered areas and ~8 s for those elsewhere. For P waves, the period of reliable waveforms extends to 5 s.

We measured the frequency-dependent phase anomalies between the synthetic and recorded seismograms in several narrow frequency bands (0.0125–0.025, 0.025–0.05, 0.05–0.1, 0.1–0.2 Hz) and a broad frequency band (0.0125–0.2 Hz) by waveform cross-correlation. For the same arrival (say, Pn), we made measurements on all useful components of the three-component records, since the different components of the same arrival provide independent constraints on the Earth structure (Shen et al., 2008). Figure 5 shows an example of the band-pass-filtered observed and synthetic Pn and Rayleigh waveforms. We obtained over 2,400 high-quality measurements for the various arrivals, frequency bands, and components.

In order to compute the Fréchet kernels of the measurements with respect to the model parameters, we have adopted the strain Green tensor (SGT) database approach developed by Zhao et al. (2005; 2006). We have calculated the receiver strain Green tensors (RSGTs) for the 16 stations we have selected in the INSN network as well as the source strain Green tensors (SSGTs) for 31 events (see Zhao et al. 2006 for details of the Fréchet kernels using the RSGTs and SSGTs). The numerical calculations were carried out with 45 processors on the Linux cluster at URI/GSO. The resulting SGT database occupies a disk space of about 13 Terabytes. The Fréchet kernels for all the measurements can be efficiently calculated using the SGTs in the database in an iterative full-wave, finite-frequency 3D tomography for the Iran region.

Figure 6 shows an example of the sensitivity kernels for the Pn and Rayleigh waves in Figure 5. Note the sensitivities of the Pn traveltimes to S wave speed. To a lesser extent, the Rayleigh wave phase is also affected by the P wave speed near the surface. Using numerical and analytical solutions, Zhang and Shen (2008) show that for finite-frequency waves, S wave-speed perturbations may have significant effects on P waveforms. At short source-receiver distances and near the source and receiver, the cross-dependence of P waveforms on S wave-speed is substantial. This finite-frequency effect has important implications for seismic tomography, particularly for regional and local earthquake tomography, in which the volume of interest is often within several 10 s of wavelength from receivers or both sources and receivers. Even for regions far from sources and receivers, neglecting this cross-dependence means that the estimates of the P wave-speed near the source and receiver are likely biased, and such errors may propagate into the rest of the model in tomographic inversions.

CONCLUSIONS AND RECOMMENDATIONS

We have made great efforts in developing and validating finite-frequency sensitivity kernels for 3D velocity and attenuation reference models. We have implemented a non-staggered-grid finite-difference algorithm in spherical geometry which allows us to conduct full-wave, finite-frequency non-linear 3D tomography in a large region where the Earth's sphericity effect on seismic wave propagation cannot be neglected. We have calculated the strain Green tensors for the INSN stations and selected earthquakes. Using waveform cross-correlation, we measured over 2,400 body and surface wave phase anomalies relative to synthetic waveforms of an initial 3D reference model. We are applying the full-wave-field kernels to obtain a refined 3D model for the Iran region. Finally, substantial efforts are needed to further develop the method for large-scale 3D models and models with anisotropy.

REFERENCES

- Asudeh, I. (1982). Pn velocities beneath Iran, *Earth Planet. Sci. Lett.* 61: 136–142.
- Chapman, C. H., and J. A. Orcutt (1985). The computation of body wave synthetic seismograms in laterally homogeneous media, *Rev. Geophys.* 23: 105–163.
- Chen, C.-Y., W.-P. Chen, and P. Molnar (1980). The uppermost mantle P-wave velocities beneath Turkey and Iran, *Geophys. Res. Lett.* 7: 77–80.
- Hearn, T. and J. Ni (1994). Pn velocities beneath continental collision zones: The Turkish-Iranian plateau, *Geophys. J. Int.* 117: 273–283.
- Maggi, A., and K. Priestley (2005). Surface waveform tomography of the Turkish-Iranian plateau, *Geophys. J. Int.* 160: 1068–1080.
- Olsen, K.B. (1994). Simulation of three-dimensional wave propagation in the Salt Lake Basin, Ph.D. Thesis, University of Utah, Salt Lake City, Utah, 157p.
- Pasyanos, M. E., W. E. Walter, M.P. Flanagan, P. Goldstein, and J. Bhattacharyya (2004). Building and testing an *a priori* geophysical model for western Eurasia and North Africa, *PAGEOPH*, 161, 235–281.
- Ritzwoller, M.H., M.P. Barmin, A. Villasenor, A.L. Levshin, and E.R. Engdahl (2002). Pn and Sn tomography across Eurasia to improve regional seismic event locations, *Tectonophysics* 358: 39–55.
- Ritzwoller, M. H., and A. Levshin (1988). Eurasian surface wave tomography: Group velocities, *J. Geophys. Res.* 103: 4839–4878.
- Ritzwoller, M. H., A. Levshin, L. Ratnikova, and A. Egorkin (1988). Intermediate-period group-velocity maps across Central Asia, western China, and parts of the Middle East, *Geophys. J. Int.* 134: 315–328.
- Shen, Y., Z. Zhang, and L. Zhao (in press). Component-dependent Fréchet sensitivity kernels and utility of three-component seismic records, *Bull. Seism. Soc. Am.*
- Walter, W. R., M.E. Pasayanos, J. Bhattacharyya, and J. O'Boyle (2000). MENA 1.1 – An updated Geophysical regionalization of the Middle East and North Africa, UCRL-ID-138079, Lawrence Livermore National Laboratory Report.
- Zhang, Z., and Y. Shen (in press). Cross-dependence of finite-frequency compressional waveforms to shear seismic wave-speeds, *Geophys. J. Int.*
- Zhao, L., P. Chen, and T.H. Jordan (2006). Strain Green tensor, reciprocity, and their applications to seismic source and structure studies, *Bull. Seism. Soc. Am.* 96: 1753–1763, doi:10.1785/0120050253.
- Zhao, L., T.H. Jordan, and K.B. Olsen, and P. Chen (2005). Fréchet kernels for imaging regional earth structure based on three-dimensional reference models, *Bull. Seism. Soc. Am.* 95: 2066–2080.

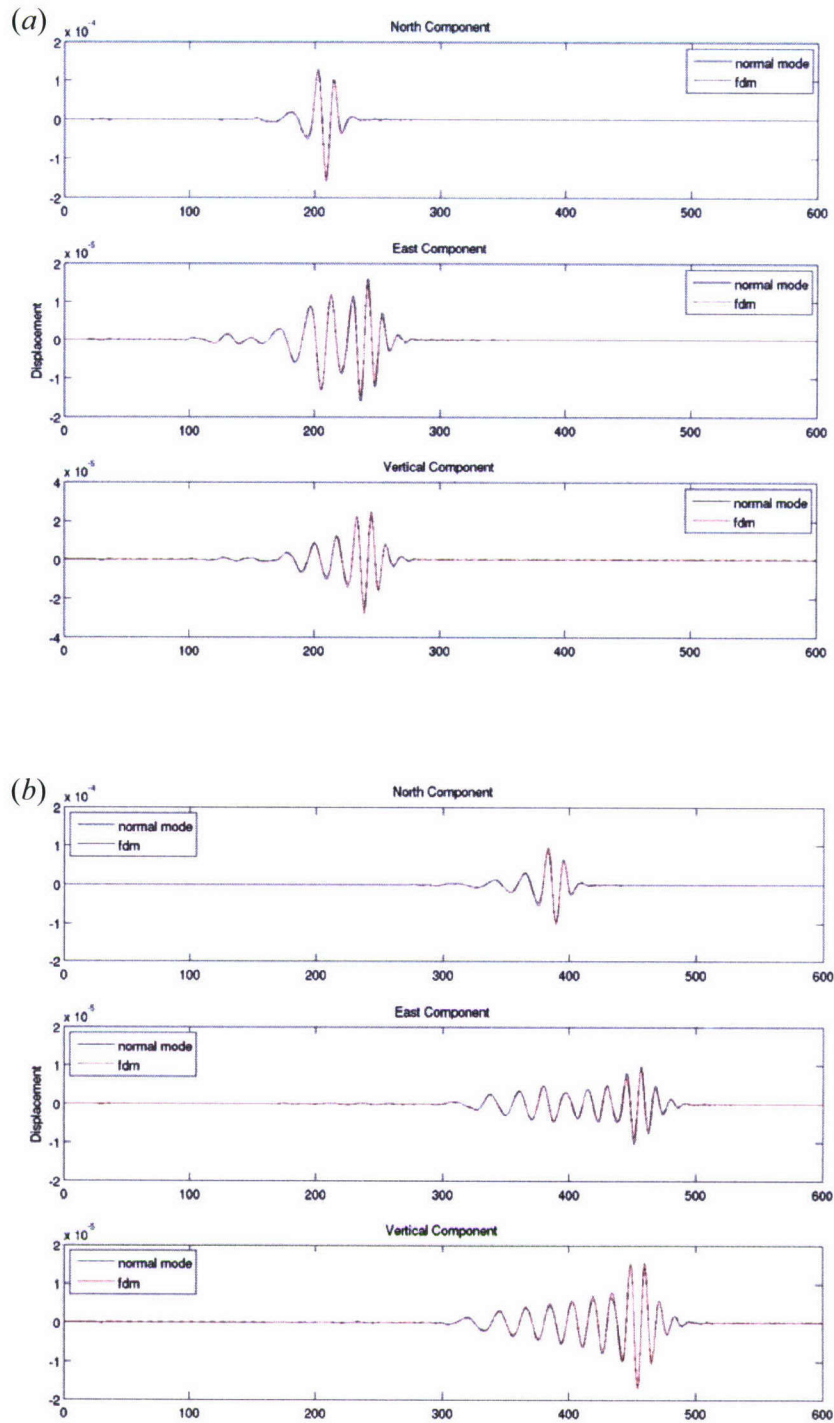


Figure 1. Comparisons between two sets of 3-component synthetics calculated by the spherical finite-difference algorithm developed in this study and by normal-mode summation. These are for a surface source located on the equator with strike, dip and rake angles of 45°, 45° and 45°, respectively, and surface receivers to the east of the source at 5° (a) and 10° (b) distances.

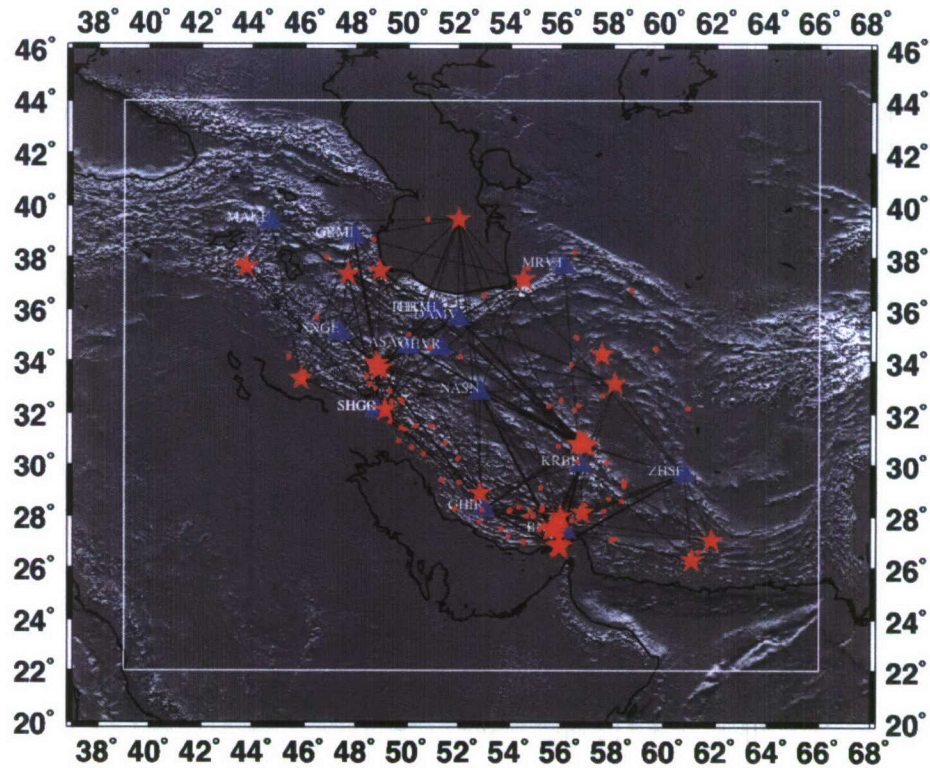


Figure 2. Relief map of the Iran region under study. Red stars show the epicenters of the 31 selected earthquakes, and blue triangles show the INSN stations used in our tomography inversions. Small red dots mark the locations of the earthquakes, for which we have collected waveforms. Our modeling volume is in the area outlined by the rectangle and has a depth range of 0 to 700 km.

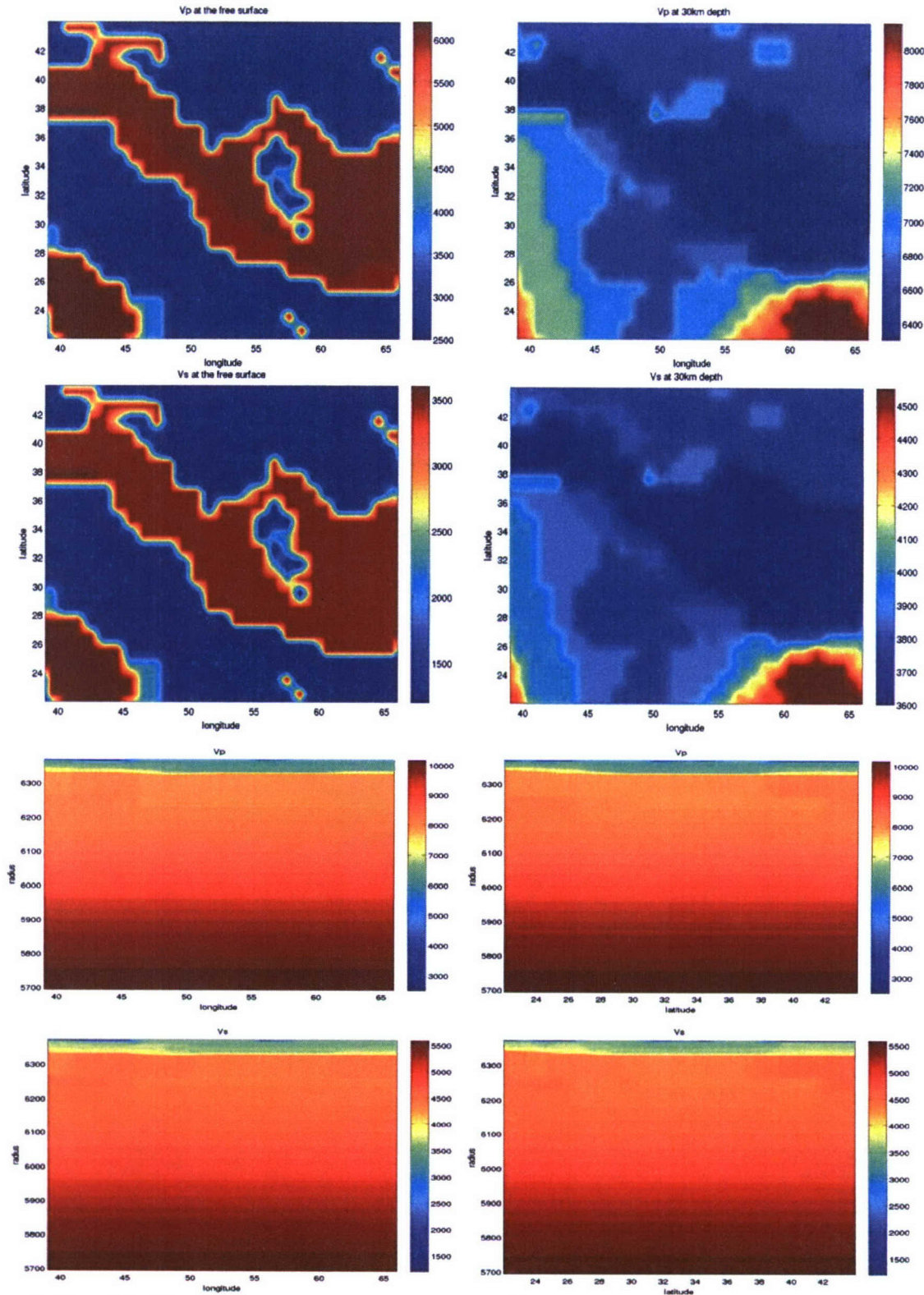


Figure 3. Plots of the 3D reference model (Pasyanos et al. 2004). (1st row) Map views of V_p at 0 km and 30 km depths. (2nd row) Map views of V_s at 0 km and 30 km depths. (3rd row) Profiles of V_p along 34°N and 57°E. (4th row) Profiles of V_s along 34°N and 57°E.

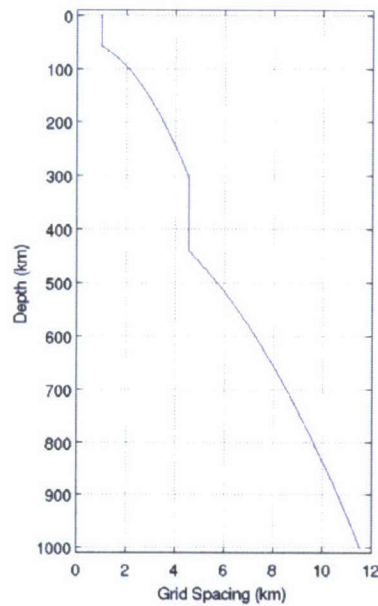


Figure 4. Depth variation of the radial grid size used in the spherical non-uniform grid finite-difference simulations in the 3D reference model.

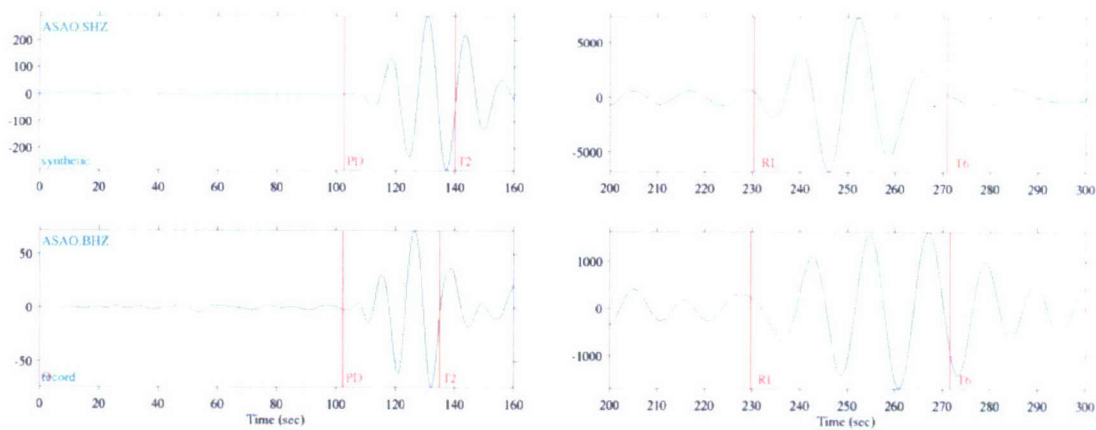


Figure 5 Pn (left panels) and Rayleigh (right panels) waves from 14 May, 2005 earthquake ((Lat. 120.773, Long. 56.899) recorded on the vertical component at station ASAO (Figure 2). The synthetic waveforms calculated using the finite-difference code in a spherical coordinate system (top traces) are plotted for comparison. The waveforms have been band-pass filtered between 0.05-0.1 Hz. The vertical lines mark the time windows, within which cross-correlation measurements and corresponding sensitivity kernels (Figure 6) are calculated.

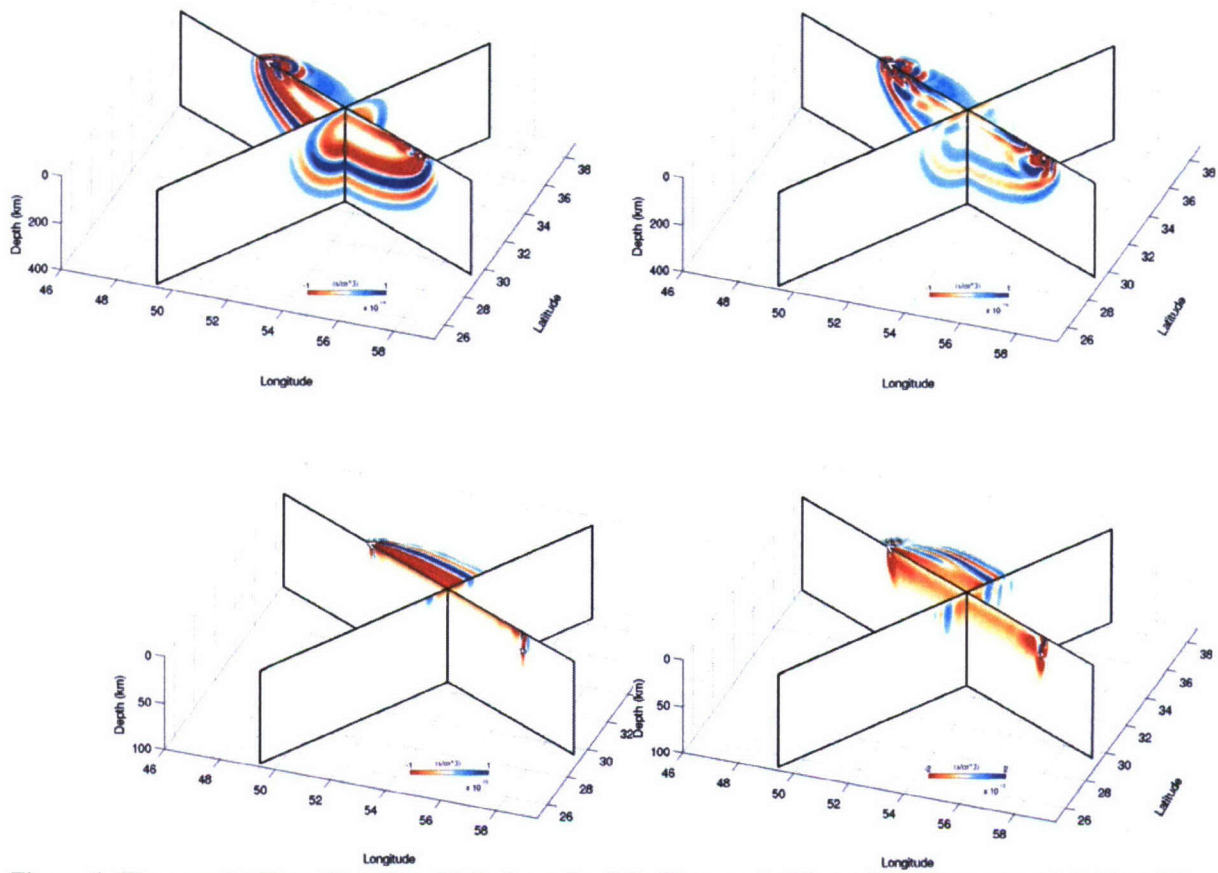


Figure 6 (Top panels) Traveltime Sensitivity kernels of the Pn wave in Figure 5 to P wave-speed (left) and S wave-speed (right) perturbations. The kernels are so defined that low-velocity anomaly in the negative sensitivity region (red colors) results in a phase delay, while the same anomaly in the positive sensitivity region corresponds to an earlier arrival. (Lower panels) Phase sensitivity kernels of the Rayleigh wave in Fig. 5 to P wave-speed (left) and S wave-speed (right) perturbations. Note the vertical and color scales are different from those for the Pn wave.